

Soft Matter

Accepted Manuscript

This article can be cited before page numbers have been issued, to do this please use: M. Cordova-Gonzalez, P. Bazazi and S. H. Hejazi, *Soft Matter*, 2026, DOI: 10.1039/D6SM00195E.



This is an Accepted Manuscript, which has been through the Royal Society of Chemistry peer review process and has been accepted for publication.

Accepted Manuscripts are published online shortly after acceptance, before technical editing, formatting and proof reading. Using this free service, authors can make their results available to the community, in citable form, before we publish the edited article. We will replace this Accepted Manuscript with the edited and formatted Advance Article as soon as it is available.

You can find more information about Accepted Manuscripts in the [Information for Authors](#).

Please note that technical editing may introduce minor changes to the text and/or graphics, which may alter content. The journal's standard [Terms & Conditions](#) and the [Ethical guidelines](#) still apply. In no event shall the Royal Society of Chemistry be held responsible for any errors or omissions in this Accepted Manuscript or any consequences arising from the use of any information it contains.

Dynamics of emulsion drop impact, spreading and evaporation: Effect of internal phase gelation

Mario Cordova-Gonzalez,[†] Parisa Bazazi,^{*,‡} and S. Hossein Hejazi^{*,†}

[†]*Department of Chemical and Petroleum Engineering, University of Calgary, Calgary, AB T2N 1N4, Canada*

[‡]*Department of Petroleum Engineering, Colorado School of Mines, Golden, USA*

E-mail: pbazazi@mines.edu; shhejazi@ucalgary.ca

Abstract

The dynamics of drop impact, spreading, and evaporation on solid surfaces are fundamental to many processes, including agricultural spraying, printing, combustion, and coating. While these behaviors are well understood for single phase liquids, less is known about emulsions with complex internal structures. Here, we report an experimental study on the dynamics of water-in-oil emulsion droplets containing either liquid or gelled aqueous phases. The continuous phase is composed of *n*-heptane and Span 80 micelles, while the dispersed phase is a reactive sodium silicate–ammonium bicarbonate solution that undergoes gelation. Internal gelation changes the rheological response of the dispersed phase and is therefore to modify dissipation during spreading and drying. During the impact stage, the dynamics are similar for both emulsion types within our experimental resolution, whereas during the subsequent spreading stage gel-containing emulsions reach smaller wetted areas. Measured maximum spreading factors are broadly consistent with unified inertial–capillary–viscous scaling for water emulsions, while gel emulsions show systematic deviations at higher internal-phase fractions. Bottom-view fluorescence imaging reveals distinct drying patterns: isolated



circular deposits for water emulsions and rugged, interconnected structures for gel emulsions. These findings highlight the importance of internal droplet structure in governing impact and drying dynamics, with implications for a wide range of emulsion-based technologies.

Keywords: Drop impact and spreading, Reactive emulsions, Aqueous phase gelation, Evaporation, Drying patterns, Deposit morphology

1. INTRODUCTION

The impact, spreading, and evaporation of liquid drops on solid surfaces play a critical role in many natural and industrial processes, including agricultural spraying, cooling, enhanced oil recovery, combustion, hydrogel formation, drop-by-drop printing, coating, and drug delivery.^{1–11} Multiphase liquid drops, such as emulsions, may contain complex internal structures that influence impact dynamics and, consequently, modify spreading and evaporation behavior. Key contributing factors include changes in apparent viscosity, interactions between the dispersed phase and the solid substrate, capillary effects at internal interfaces, and a reduction in the evaporation rate of the continuous phase.^{12–15} Additionally, gelation of the internal phase is widely used in drug delivery applications, where a liquid phase transforms into a gel to support the transport and controlled release of pharmaceuticals.^{16,17} These systems represent tunable soft materials where internal rheological transitions can be exploited to control droplet behavior on surfaces.

The liquid-to-gel transition of the internal phase, combined with the impact, spreading, and evaporation of emulsion drops, presents new opportunities for material processing applications such as printing, coating, and transport in porous media. Emulsion-based impact studies are especially relevant for non-contact dispensing of solidifying materials onto solid substrates. However, the influence of internal phase gelation on the complete sequence of impact, spreading, and evaporation remains underexplored, largely due to difficulties in



20 controlling gel-phase deposition.

21 The impact stage governs the initial droplet morphology and wetted area, influenced
22 by parameters such as impact velocity, surface temperature, and fluid properties.^{18–20} For
23 instance, emulsions with low dispersed-phase volume fractions and high Weber numbers (the
24 ratio of inertial to surface tension forces) tend to splash, expelling fluid outward.¹² Following
25 impact, the droplet spreads until it reaches a maximum diameter.^{21,22} Gelled emulsions may
26 either enhance or suppress spreading, depending on interfacial adsorption and the volume
27 fraction of the internal phase.

28 Finally, the continuous phase, which is typically a volatile solvent or fuel, evaporates.²³
29 During this stage, solidified internal droplets may constrain contact line retraction, reduce
30 evaporation rates, or generate patterned deposits.¹⁵ The overall deposition outcome is there-
31 fore influenced by the internal liquid-to-gel transition. A detailed investigation of these
32 dynamics is needed to understand how internal gelation influences each stage and shapes the
33 final deposition outcome.

34 In this article, we investigate the impact, spreading, and evaporation dynamics of water-
35 in-oil emulsions on solid surfaces. The emulsions are composed of a continuous oil phase
36 (n-heptane with Span 80) and a dispersed phase consisting of either deionized water or a
37 reactive mixture of sodium silicate and ammonium bicarbonate. In the former case, the
38 dispersed phase remains liquid; in the latter, it undergoes a sol-gel transition. The gelation
39 process leads to physicochemical transformations that measurably affect droplet spreading,
40 evaporation, and final deposit morphology. Understanding the relationship between inter-
41 nal phase transitions and drop deposition is essential for applications that require precise
42 placement of gelled emulsions, where interfacial flow behavior governs the distribution of
43 deposited material.



2. EXPERIMENTS

2.1 Materials

We used a sodium silicate solution (10.6 wt.% Na₂O and 26.5 wt.% SiO₂, Sigma-Aldrich) as the silica gel precursor and an ammonium bicarbonate dried powder as a reactant (Reagent-Plus, 99.0 %, Sigma-Aldrich CAS 1066-33-7). We employed *n*-heptane (99 %, Sigma-Aldrich CAS 142-82-5) as the main organic phase and a non-ionic surfactant Sorbitane monooleate (Span-80, CAS 1338-43-8) as the micellar source.

2.2 Preparation and characterization of aqueous solutions

We prepared a 2.0 wt.% sodium silicate solution and ammonium bicarbonate solutions at concentrations of 1.1 wt.%, 2.2 wt.%, 2.7 wt.%, 3.3 wt.%, and 4.4 wt.%. Equal volumes of the sodium silicate and ammonium bicarbonate solutions were mixed (1:1 volume ratio), resulting in the formation of a silica gel via a sol-gel reaction through hydrolysis and condensation-polymerization.²⁴⁻²⁷ Throughout this manuscript, we refer to this mixture as the reactant solution. The sample containing 4.4 wt.% ammonium bicarbonate is the only one that no longer flows shortly after preparation, as shown by the inverted bottle at 0.16 hours in **Figure 1(b)**, and this concentration is used throughout our study.

We measure the shear rheology of all the samples with a rotational shear rheometer (Discovery Hybrid Rheometer HR 30, TA Instruments) equipped with a concentric cylinder geometry of a 30 mm diameter cup and a DIN rotor with an aluminum bob (28 mm diameter and 42 mm length). The sample is loaded within the cup's annular volume (12 mL) and immediately set to the operating gap (2 mm). The temperature is set to 21 °C for all the measurements which is controlled by a Peltier system. To minimize evaporation, we cover the top of the cylinder with two semi-circle plates at a reasonable distance from the rotating bob to avoid direct contact during the tests. First, we conduct a series of continuous oscillation tests in the aqueous mixtures to find out the timing for gel formation and identify the sol-gel



69 transition over 24 hours. The samples are subjected to a controlled shear strain, with con-
70 stant angular frequency, $\omega = 10$ (rad/s), and oscillatory strain, $\lambda = 1.0$ %. We compute the
71 complex viscosity, i.e. the complex modulus divided by the applied frequency, as an indicator
72 how strong and fast the sample is deformed during the oscillation test.²⁸ **Figure 1(c)** shows
73 that samples containing 4.4, 3.3, 2.7, and 2.2 wt.% ammonium bicarbonate exhibit initially
74 constant complex viscosities, which begin to increase at approximately 0.16, 1, 2, and 6 h,
75 respectively. This increase indicates the onset of the sol-gel transition associated with the
76 growth and aggregation of silica clusters.²⁵ Ultimately, the complex viscosity values reach
77 a plateau at about 24 hours. The sample containing 1.1 wt.% of ammonium bicarbonate
78 never forms a gel due to the low concentration, instead, colloidal particles of sodium silicate
79 behave as discrete species.²⁹ **Figure S1**, confirms the sol-gel transition times through the
80 crossover of the viscous (G') and elastic (G'') modulus.²⁸ The gel formation process starts
81 when the elastic behaviour of the solution becomes more dominant. Since the formulation
82 with the combination of 2.0 wt.% sodium silicate and 4.4 wt.% reactant becomes the most
83 rigid gel within 0.16 h without breaking, it is selected to create the gel emulsions in this
84 study.

85 2.3 Oil solution preparation

86 The oil phase, referred to as the micellar solution, consists of 5 wt.% Span-80 (Sigma-Aldrich)
87 in *n*-heptane and is used to form water-in-oil (W/O) emulsions.^{30–35} The critical micelle
88 concentration (CMC) of Span-80 in *n*-heptane is reported to be approximately 0.018 mM.³⁶
89 In this study, we use 5 wt.% Span-80, corresponding to a concentration several orders of
90 magnitude above the CMC. At this high concentration, the oil phase contains an abundance
91 of reverse micelles, ensuring that surfactant availability is not limited by bulk depletion.
92 This condition favors rapid coverage of newly created interfaces and enables the formation
93 of aqueous nanodomains³² capable of hosting reactants, which is essential for the spontaneous
94 emulsification and subsequent gel formation investigated here.



95 2.4 Emulsion preparation

96 Emulsification procedure involves adding the aqueous phase, either deionized (DI) water or
97 a freshly prepared reactant solution containing 4.4 wt.% ammonium bicarbonate, to the mi-
98 cellular solution. The mixture is then sonicated for 1 minute using an ultrasonic probe at 100%
99 amplitude. Emulsions are stabilized by amphiphilic Span-80 micelles, which entrap aque-
100 ous nanodomains containing the sol-gel precursors within their inner cores, facilitating gel
101 formation inside confined microdroplets.^{37,38} When the silicate precursor reacts with ammo-
102 nium bicarbonate, silica polymerization is initiated, leading to the growth and aggregation of
103 silica clusters. This process gradually forms soft, gel-like particles within the dispersed inner
104 phase, while the emulsion remains suspended in a continuous *n*-heptane phase.¹⁵ The onset
105 of gelation, indicated by the rise in G' (≈ 6 minutes), precedes the $G'-G''$ crossover (≈ 9.6 min-
106 utes) by approximately 3–4 minutes (**Figure S1a**), indicating a short but finite viscoelastic
107 transition regime. Because the emulsification time is significantly shorter than the gelation
108 time, the dispersed aqueous droplets remain fully liquid during emulsion formation.

109 After sonication, the emulsions are stirred at 250 rpm for 1 h to maintain homogene-
110 ity while the sol-gel transition proceeds to completion. The gel emulsions studied here,
111 therefore, consist of fully gelled aqueous droplets dispersed in oil, rather than suspensions
112 of solid particles formed prior to emulsification. Droplet impact experiments are performed
113 immediately after stirring is stopped (“freshly prepared” state). From sample loading to
114 completion of the impact measurements requires less than one minute; thus, impact ex-
115 periments are conducted after gelation is complete (gel emulsions) or with a liquid internal
116 phase (water emulsions). The mean dispersed-phase droplet diameter for all emulsion systems
117 is 280 ± 35 nm, as previously reported.¹⁵ For this study, emulsions are prepared with 5, 10,
118 and 25 vol.% aqueous phase.



119 2.5 Emulsion characterization

120 We measure the density of the emulsion samples with a portable density meter (DMA 35,
121 Anton Paar) after 1 hour of sample preparation and stirring. The densities are constant
122 and equal to 0.724 ± 0.05 and 0.720 ± 0.05 (g/mL), for water and gel emulsions at 10 vol.%
123 aqueous phase, respectively. Surface tension at the liquid–air interface was measured using
124 a drop shape analyzer (DSA 100, Krüss Instruments). The equilibrium surface tensions of
125 *n*-heptane and the micellar solution were measured to be 20.10 mN/m and 16.31 mN/m,
126 respectively. For all water and gel emulsion droplets, the equilibrium surface tension was
127 approximately 16 mN/m. Finally, we capture fluorescence images of residual emulsion sam-
128 ples, after the evaporation of *n*-heptane, using confocal laser scanning microscopy (Nikon
129 A1R), with a 2x and 10x magnification lens at 1024 x 1024 pixels and 2048 x 2048 pixels,
130 respectively. We deposit drops of water and gel emulsions with a fixed volume of 0.1 μ L
131 on a glass slide exposed to air to let the solvent evaporate. We add a fluorescent dye to
132 the oil phase at 0.1 wt.% (Kingscote red dye, model 506, 250-R4, Cole-Parmer Canada) and
133 illuminate the drops with a 488 nm (FITC) laser emission at 10 mW power and with a fixed
134 pinhole of 1.2 AU.

135 2.6 Drop impact and spreading experiments

136 The experimental setup consists of a hydrophilic glass slide (VWR, VistaVision) with a
137 known contact angle placed on an automated dosing stage (DSA 100, Krüss Instruments)
138 coupled to a monochrome camera (CF03, Krüss Instruments), as sketched in **Figure 1(a)**.
139 The camera is perpendicular to the glass substrate with a 2° inclination. The dosing system
140 incorporates a glass syringe and a 0.5 mm diameter stainless steel needle placed 30 mm above
141 the substrate. A drop is formed by injecting at 0.2 μ L/s until the drop detaches from the
142 needle and impacts the glass surface. The injected volume for drop release is kept constant at
143 5.6 μ L for heptane and 5.2 μ L for all other liquids, producing drops with an initial diameter
144 of $D_0 = 2.20 \pm 0.05$ mm for heptane and $D_0 = 2.15 \pm 0.05$ mm for the remaining tests.



145 The impact velocity in all tests is approximately 0.60 ± 0.05 m/s, computed from frames
 146 immediately before impact. The side-view images of the drop are captured by the camera
 147 at 1000 fps and a resolution of 38 pixels/mm. The size of acquired images is 600 x 80 pixels
 148 and they are processed in ImageJ to obtain the time evolution of the droplet diameter, $D(t)$.

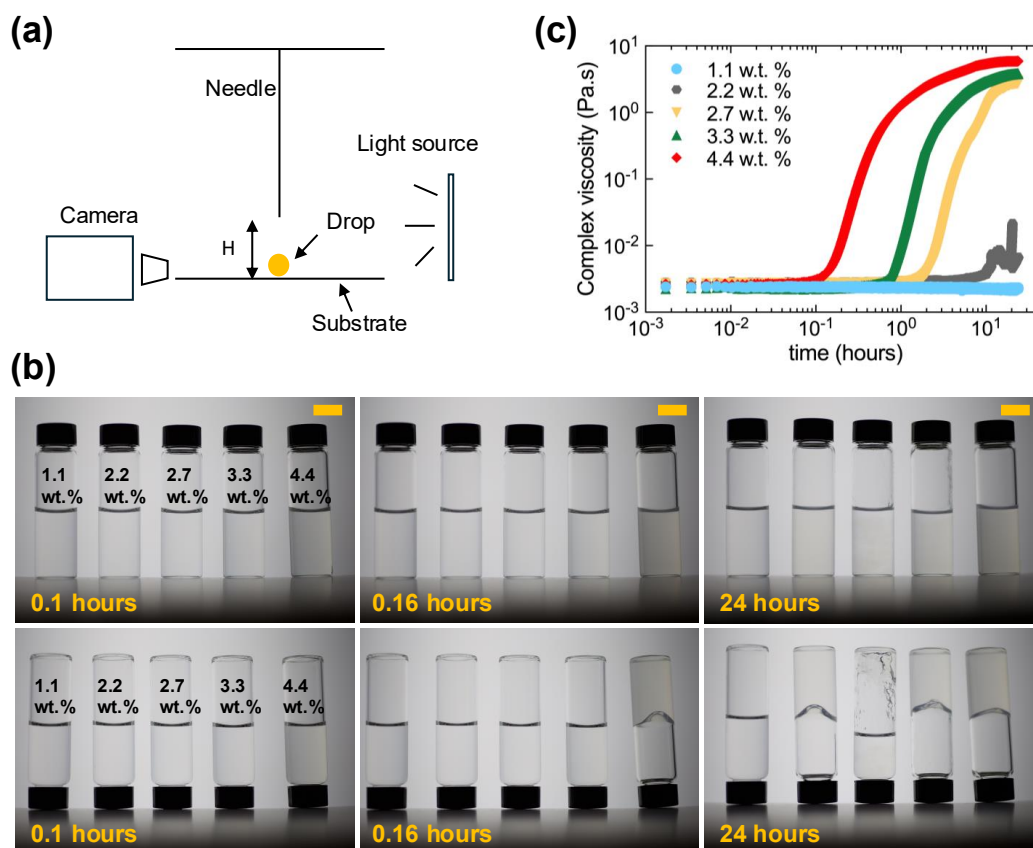


Figure 1: Schematic illustration of the experimental setup and gel formation process. (a) A glass substrate is placed on a flat surface adjacent to a monochrome camera. Drops are injected at a constant flow rate of $0.2 \mu\text{L/s}$ from a height of 30 mm above the glass substrate. The injected volume is $5.6 \mu\text{L}$ for *n*-heptane and $5.2 \mu\text{L}$ for all other cases. The drop detaches from the needle, falls under gravity, impacts the solid surface, and spreads. (b) Visual representation of gel formation in samples prepared with 2.0 wt.% sodium silicate and 1.1, 2.2, 2.7, 3.3, and 4.4 wt.% ammonium bicarbonate, along with corresponding images of inverted bottles. The scale bar represents 1 cm. (c) Oscillation tests performed on all samples shown in (b) at a fixed shear strain of $\lambda = 1.0\%$ and an angular frequency of $\omega = 10$ rad/s. The onset of gelation is identified by the increase in complex viscosity. Gel formation at 4.4 wt.% occurs at 0.16 h and reaches the highest complex viscosity magnitude. All tests were conducted at room temperature (21°C).



3. RESULTS AND DISCUSSION

3.1 Single phase liquids: Heptane and micellar solution

We first investigate the impact, spreading, and evaporation dynamics of emulsion-free drops. We then extend this analysis to emulsion-laden drops to examine the influence of dispersed aqueous phases on the overall dynamics. **Figure 2(a)** and **2(b)** show the impact, spreading, and evaporation of a drop composed of pure *n*-heptane (surfactant-free) and the micellar solution (surfactant-loaded), respectively. Initially, the drop falls under gravity until it contacts the solid surface. Upon impact, the drop wets an initial area with a diameter denoted as D_i , which we define at $t = 1$ ms. The drop then rapidly spreads due to the impact, reaching a maximum wetted diameter D_{\max} . At this stage, the drop exhibits a toroidal shape with an air cavity at its center while the outer rim remains continuous. This shape results from capillary waves generated at impact, which propagate along the drop surface.^{39,40} The vertical kinetic energy at impact is transferred into radial motion, driving the lateral spread of the drop.⁴¹ As the cavity collapses, the drop edges retract due to the restoring force of the liquid–air interface. The impact behavior is identical for both the *n*-heptane and micellar solution drops, as shown in **Figure 2(a)** and **2(b)**.

The early-stage spreading is governed by inertial momentum transfer, with a characteristic timescale $\tau_{\text{inert}} \sim D_0/U_0$, where $D_0 \approx 2.15$ mm is the initial droplet diameter and $U_0 \approx 0.6$ m/s is the impact velocity. This yields a timescale on the order of a few milliseconds under our impact conditions. In contrast, surfactant effects require interfacial equilibration, which involves finite adsorption and molecular rearrangement processes, including monomer exchange with micelles and adsorption at the newly created interface. Although the surfactant concentration used here is far above the CMC ($\approx 880 \times$ CMC), implying that bulk depletion is not limiting, interfacial equilibration may still occur on timescales longer than τ_{inert} . Consequently, surfactant-mediated changes in interfacial properties are not expected to influence the very early, inertia-dominated spreading stage, consistent with our obser-



175 vations. After the impact phase, the drop continues to spread and eventually reaches a
176 maximum spreading diameter, $D_{S_{\max}}$. The wetting film of the micellar solution drop extends
177 2 mm farther than that of the surfactant-free drop.

178 During impact on the glass substrate, a thin liquid film forms as the drop spreads. Be-
179 cause *n*-heptane evaporates rapidly, the film thins quickly and the contact line recedes once
180 the maximum spreading diameter is reached. Surfactant-free droplets retract and evaporate
181 uniformly, leaving no visible residues (**Figure 2(a)**). In contrast, droplets containing high
182 concentrations of Span-80 consistently leave sub-millimetric sessile droplets at the periph-
183 ery of the wetted region (**Figure 2b**). The formation of these peripheral droplets likely
184 reflects a combination of mechanisms rather than surfactant accumulation alone. Although
185 surface-active molecules migrate toward the interface during spreading and retraction, the
186 adsorption kinetics of Span-80 in a nonpolar solvent are relatively slow, suggesting that clas-
187 sical Marangoni flows may not fully account for the observed deposition. Instead, the rapid
188 evaporation of heptane may induce strong thermal gradients and accelerate film thinning,
189 bringing the liquid layer into a regime where van der Waals forces and disjoining pressure
190 promote rupture. Since both droplets have comparable volumes, the micellar droplet is cor-
191 respondingly thinner than the heptane droplet and spreads over a larger surface area. This
192 increased interfacial area promotes faster evaporation of the micellar solution compared to
193 the heptane droplet.



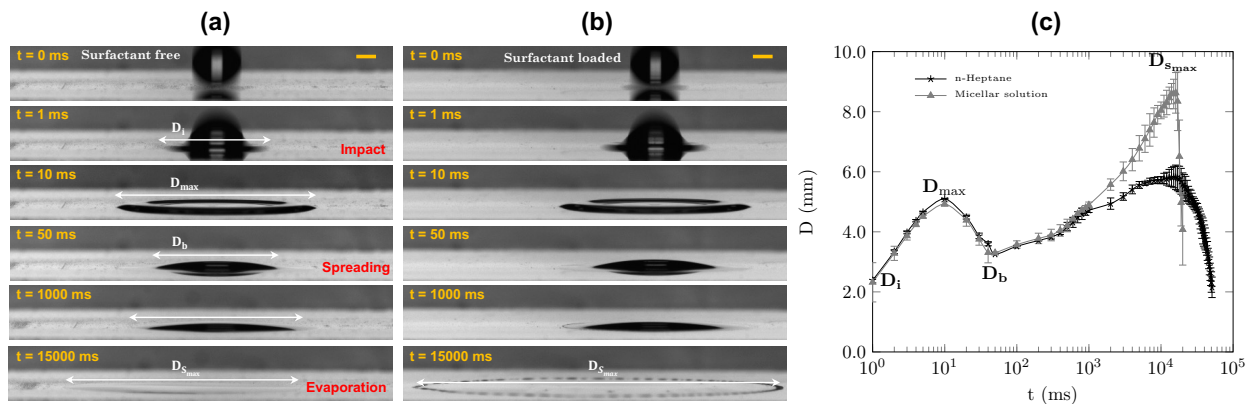


Figure 2: Impact, spreading, recoil, and evaporation dynamics of (a) a surfactant-free *n*-heptane drop and (b) a surfactant-loaded micellar solution (5 wt.% Span-80 in *n*-heptane). Time-resolved images (0–15000 ms) illustrate the successive stages of impact, spreading, recoil, and evaporation. The initial droplet volume is $5.6 \mu\text{L}$ for *n*-heptane and $5.2 \mu\text{L}$ for the micellar solution. The scale bar represents $750 \mu\text{m}$. (c) Temporal evolution of the droplet diameter D for *n*-heptane (asterisk markers) and the micellar solution (solid triangular markers). D_i denotes the droplet diameter at initial contact with the substrate; D_b corresponds to the recoiling diameter after maximum spreading; D_{max} is the maximum wetted diameter during the impact stage; and $D_{S_{max}}$ represents the maximum spreading diameter attained during the evaporation stage ($t = 15000$ ms). The subsequent decrease in diameter reflects solvent evaporation.

194 3.2 Two phase systems: water-emulsions and gel-emulsions

195 We next focus on emulsion-laden drops to explore the role of internal phase heterogeneity in
 196 shaping drop dynamics. **Figure 3(a)–(c)** shows the time sequence of impact, spreading, and
 197 evaporation for three cases: emulsion-free, water emulsion, and gel emulsion drops. While
 198 the drops adopt similar morphologies during the impact phase, the maximum spreading
 199 diameter, $D_{S_{max}}$, is reduced in both water and gel emulsion drops compared to the emulsion-
 200 free case. This reduction in $D_{S_{max}}$ is also observed in drops with higher aqueous phase
 201 volumes (10 and 25 vol.%), as shown in **Figure S2** and **Figure S3**, respectively.

202 To examine whether the spreading dynamics can be collapsed onto a universal form,
 203 we rescale the droplet diameter as D/D_{max} and the time as t/τ , where $\tau = D_{max}/U_0$ is
 204 the characteristic inertial spreading time. This normalization has been shown to collapse
 205 the spreading dynamics of Newtonian and non-Newtonian droplets over a wide range of



206 conditions.⁴² **Figure 3(d)** presents the temporal evolution of the scaled drop diameter for
207 the emulsion-free drop (i.e., micellar solution) in gray and for drops with water (blue) and
208 gel emulsions (red) at 5, 10, and 25 vol.% aqueous phase. Applying this rescaling to our data
209 (**Figure 3d**), we find that the early-time spreading dynamics up to the point of maximum
210 impact area ($D/D_{\max} = 1$) collapse for the single-phase liquids as well as for water and gel
211 emulsions across the investigated concentration range.

212 These results indicate that the proposed rescaling, previously shown to describe inertial
213 spreading in single-phase droplets, remains applicable during the spreading regime of emul-
214 sions. In particular, the collapse observed during the spreading phase of impacting droplets
215 (up to $D/D_{\max} = 1$) is consistent with the scaling framework introduced by Gordillo et al.⁴³
216 and further discussed by Gorin et al.,⁴² in which the spreading dynamics are described by a
217 universal function $D(t)/D_{\max} = f(t/\tau)$.

218 Beyond the point of maximum impact spreading, droplets undergo retraction followed
219 by a slower secondary spreading stage. This late-time evolution depends strongly on compo-
220 sition: for higher aqueous-phase volume fractions (25 vol.%), retraction is reduced and the
221 final normalized diameter reaches a lower plateau, with gel emulsions exhibiting systemati-
222 cally smaller D/D_{\max} than water emulsions. These deviations reflect additional dissipation
223 associated with internal microstructure, which is not captured by inertial scaling alone and
224 therefore lies outside the regime of universal collapse.

225 The maximum spreading diameter, $D_{S_{\max}}$, decreases systematically with increasing in-
226 ternal phase volume fraction. A similar trend is observed for the maximum wetted diameter
227 during impact, D_{\max} . Previous studies have shown that $D_{S_{\max}}$ increases with decreasing
228 contact angle.⁴⁴ The apparent contact angle, reported in **Table S1**, is measured at the first
229 resolvable contact frame prior to significant inertial spreading using ImageJ with the Low
230 Bond Axisymmetric Drop Shape Analysis (LB-ADSA) plugin. After the droplet reaches its
231 maximum spreading diameter, the contact angle decreases below 20° , making reliable quan-
232 tification difficult; therefore, only early-time contact angles are reported. Emulsion droplets



233 exhibit a slightly higher apparent contact angle compared to the clean liquid droplet, in-
234 dicating reduced wettability. This suggests that the presence of dispersed internal droplets
235 may hinder early-stage spreading by constraining the advancing contact line. The apparent
236 contact angles are comparable for water-based and gel-based emulsions. In gel emulsions,
237 the stiffer internal droplets may restrict the mobility of the dispersed phase,^{45,46} contributing
238 to a further reduction in spreading compared to the more deformable (soft) droplets in water
239 emulsions.

240 Moreover, we repeated the experiment for a 10 vol.% aqueous phase emulsion with the
241 needle height reduced from 30 mm to 15 mm and 5 mm. The resulting impact velocities were
242 0.52 and 0.33 ± 0.05 m/s, respectively, compared to the original 0.60 ± 0.05 m/s. **Figure S4**
243 exhibits the collapse of data points up to $D/D_{\max} = 1$.

244 To investigate the role of rheology in spreading and drying behavior, we measured the
245 shear viscosity of micellar solution (emulsion-free), water emulsions, and gel emulsions at 5,
246 10, and 25 vol.% aqueous phase, as shown in **Figure 3(e)**. To investigate the role of rheology
247 in spreading and drying behavior, we examined the viscosity of water and gel emulsions at
248 5, 10, and 25 vol.% aqueous phase. **Figure 3(e)** presents the shear viscosity as a function
249 of shear rate for micellar solution (emulsion-free), water emulsions, and gel emulsions at 5,
250 10, and 25 vol.%. The micellar solution exhibits nearly constant viscosity across a wide
251 shear rate range (approximately 2.5 to 100 s^{-1}), with a slight increase at higher shear rates
252 possibly due to the onset of secondary flow effects. In contrast, both water and gel emulsions
253 display clear shear-thinning behavior. This is observed up to 100 s^{-1} for the 5 and 10 vol.%
254 samples, and across the full shear rate range for the 25 vol.% case. Shear thinning is likely
255 caused by the disruption of inter-droplet interactions or internal gel networks under shear.⁴⁷



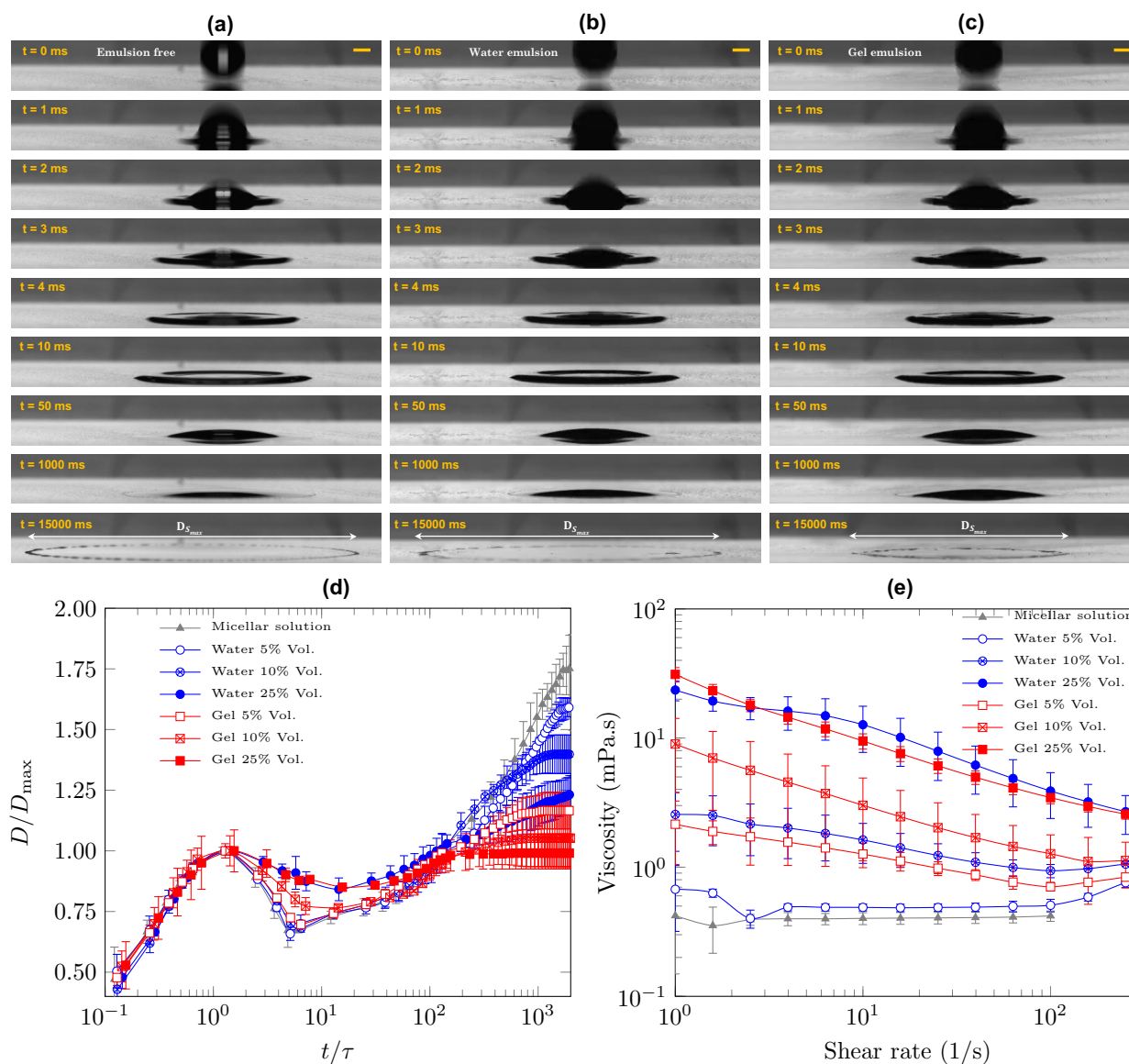


Figure 3: Impact and spreading dynamics of (a) micellar solution (emulsion-free), (b) water emulsion, and (c) gel emulsion drops at 5 vol.% aqueous phase. The injected volume is $5.2 \mu\text{L}$ for all drops. The scale bar represents $750 \mu\text{m}$. (d) Time evolution of the normalized spreading diameter D/D_{max} as a function of dimensionless time t/τ , where $\tau = D_{\text{max}}/U_0$, for micellar solution, water emulsions, and gel emulsions at 5, 10, and 25 vol.%. (e) Shear viscosity of micellar solution, water emulsions, and gel emulsions at 5, 10, and 25 vol.% as a function of shear rate.

256 The viscosity magnitude increases with higher aqueous phase content, indicating stronger
 257 inter-droplet interactions due to reduced spacing between dispersed droplets. Particularly,
 258 gel emulsions consistently exhibit higher viscosity than water emulsions at all concentrations



259 tested, which reflects the formation of internal gel structures that resist deformation. These
 260 rheological differences contribute directly to the reduced spreading observed in gel emulsions,
 261 as the more rigid internal phase offers greater resistance to flow during impact and spreading.

262 3.3 Dimensionless analysis and scaling of maximum spreading

263 The impact dynamics are characterized using the Reynolds (Re), Weber (We), and Ohnesorge
 264 (Oh) numbers, evaluated from the droplet impact conditions (**Table S2**). For the present
 265 experiments, the characteristic velocity and length scales are taken as the impact velocity
 266 $U_0 = 0.6$ m/s and the initial droplet diameter $D_0 = 2.20 \times 10^{-3}$ m for n -heptane and
 267 $D_0 = 2.15 \times 10^{-3}$ m for all other cases. The Reynolds number is calculated as $Re = \rho U_0 D_0 / \mu$,
 268 where ρ is the liquid density and μ is the dynamic viscosity. For emulsions and gel emulsions,
 269 which exhibit shear-rate-dependent viscosity, μ is evaluated at a characteristic shear rate
 270 associated with impact, approximated as $\dot{\gamma} \sim U_0 / D_0 \approx 2.8 \times 10^2$ s $^{-1}$, based on rheological
 271 measurements. The Weber number is computed as $We = \rho U_0^2 D_0 / \gamma$, where γ is the liquid
 272 surface tension. The Ohnesorge number is then obtained from $Oh = \mu / \sqrt{\rho \gamma D_0}$, which
 273 represents the relative importance of viscous effects compared to inertial and capillary forces.

274 The calculated ranges of dimensionless numbers ($Re \sim 10^2$ – 10^3 , $We \sim 10^1$, $Oh \sim 10^{-3}$ –
 275 10^{-2}) place our experiments in the inertial–capillary regime with moderate viscous influence
 276 (i.e., low-to-moderate Oh and moderate We), where maximum spreading is governed primar-
 277 ily by the balance between inertia and capillarity. Viscous dissipation becomes increasingly
 278 relevant for higher emulsion concentrations as Oh increases. In this regime, recent studies⁴⁸
 279 have shown that viscous effects can influence spreading even at relatively low Oh , consistent
 280 with the systematic reduction in spreading factor $\beta_{\max} = D_{\max} / D_0$ observed as viscosity
 281 increases.

282 We compare the measured maximum spreading factors with both classical empirical
 283 scaling laws and a unified inertial–capillary–viscous framework. A commonly used iner-
 284 tial–capillary scaling is $\beta_{\max} \sim We^{1/4}$, which neglects viscous dissipation. In addition, we



285 evaluate a smooth-transition (“unified”) correlation given by $\beta_{\max} \sim Re^{1/5} P^{1/2} / (a_1 + P^{1/2})$,
286 where $P = We Re^{-2/5}$ and $a_1 \approx 1.24^{42,49,50}$ (see **Figure 4a**). For the single-phase control
287 liquids (*n*-heptane and micellar solution), both scalings predict spreading factors in close
288 agreement with the experiments. The unified model yields $\beta_{\max} \approx 2.23$ for heptane and
289 ≈ 2.30 for the micellar solution, compared with measured values of 2.32 and 2.29, respec-
290 tively. Extending the comparison to emulsion and gel-emulsion droplets using the effective
291 viscosity evaluated at the impact-relevant shear rate shows that the inertial–capillary scal-
292 ing $\beta_{\max} \sim We^{1/4}$ predicts nearly constant spreading across all samples. Because *We* varies
293 only weakly in our experiments, this scaling cannot capture differences arising from viscos-
294 ity changes. In contrast, the unified correlation captures the overall trend of decreasing
295 spreading factor with increasing internal phase concentration.

296 For all water-emulsion samples and the 5 vol.% gel emulsion, predicted spreading factors
297 remain in close agreement with the experiments, with deviations typically within a few per-
298 cent. At higher gel-emulsion concentrations (10 and 25 vol.%), however, the unified model
299 overpredicts the measured spreading, indicating that structured internal phases introduce
300 additional dissipation not captured by a single effective viscosity. Plausible contributions
301 include internal microstructural resistance, interfacial deformation, and enhanced contact-
302 line dissipation. At higher gel concentrations, rearrangement of the internal gel droplets
303 during impact may locally increase the effective dispersed-phase volume fraction. Such tran-
304 sient concentration variations could increase dissipation and bring localized regions closer to
305 jammed conditions, thereby reducing spreading.

306 We further examine the spreading factor D_{\max}/D_0 as a function of zero-shear viscosity
307 (**Figure 4b**). Although impact occurs at high effective shear rates, μ_0 provides a sensitive
308 measure of microstructural rigidity and network strength, which correlates with additional
309 dissipation mechanisms not captured by a single effective viscosity evaluated at $\dot{\gamma} \sim U_0/D_0$.
310 A monotonic decrease in spreading with increasing zero-shear viscosity is observed. The
311 log–log representation reveals an apparent power-law trend, with distinct slopes for water



312 emulsions and gel emulsions. The steeper slope for gel emulsions suggests additional resis-
313 tance to spreading arising from internal microstructure, beyond what is captured by bulk
314 viscosity alone.

315 An alternative interpretation is to view the gel emulsions as suspensions of soft internal
316 domains dispersed within a liquid continuous phase. In this picture, the gelled aqueous
317 droplets behave as deformable inclusions that may introduce additional dissipation during
318 spreading beyond what is captured by an effective viscosity. Similar considerations arise in
319 the droplet impact of particulate suspensions, where internal microstructure and particle re-
320 arrangements modify spreading and retraction dynamics. Recent work by Shah and Driscoll
321 discusses how suspended phases in complex fluids can influence droplet impact behavior even
322 at moderate volume fractions through shear-thinning effects and microstructural rearrange-
323 ments.⁵¹ In the present system, the internal gel droplets may play a similar role by resisting
324 deformation and constraining flow within the spreading droplet.

325 Similar behavior has been reported for droplets containing rigid particle suspensions.
326 Experiments on suspension drops show that increasing particle volume fraction generally
327 reduces the maximum spreading factor due to additional dissipation arising from particle re-
328 arrangements and particle–fluid interactions during impact.^{52,53} At sufficiently high particle
329 concentrations, deviations from classical Newtonian scaling can emerge as particle inter-
330 actions and microstructural effects influence the impact dynamics.⁵⁴ Although the present
331 emulsions contain deformable gel droplets rather than rigid particles, the qualitative trends
332 observed at higher gel concentrations are consistent with the broader behavior reported for
333 suspension droplets.

334 Nevertheless, the ability of the unified framework to reproduce the overall trend of de-
335 creasing β_{\max} with increasing Oh suggests that inertia, capillarity, and viscous dissipation
336 remain the dominant controlling mechanisms. The systematic deviations observed at high
337 gel concentrations indicate the need for future extensions of the model to explicitly account
338 for multiphase and structured-drop effects.



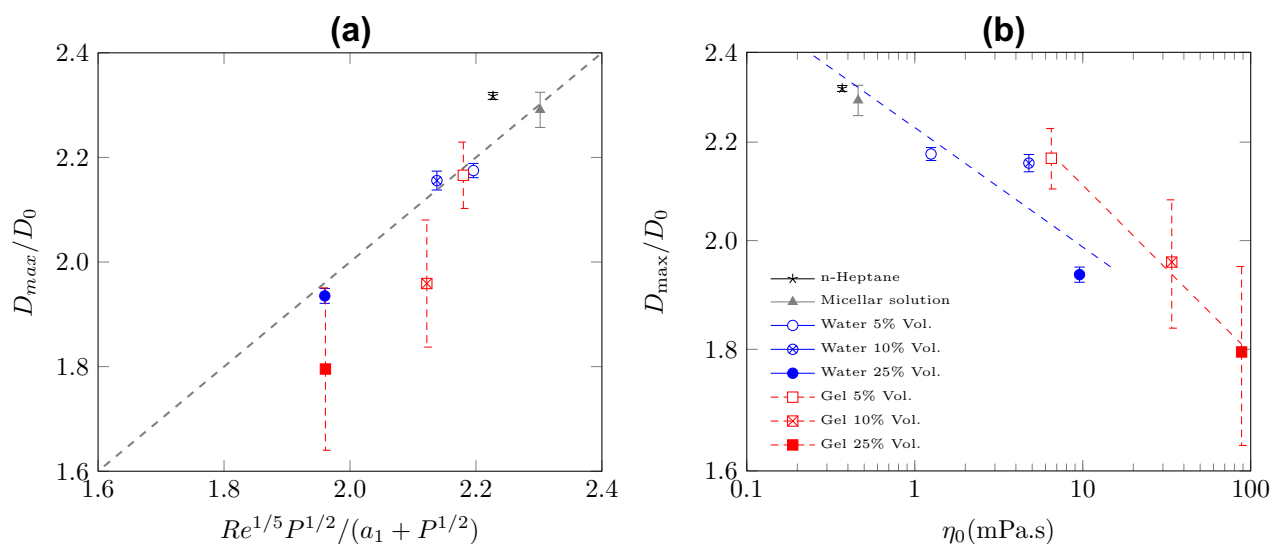


Figure 4: Maximum spreading factor D_{max}/D_0 as a function of (a) the unified correlation $Re^{1/5} P^{1/2} / (a_1 + P^{1/2})$ and (b) zero-shear viscosity (log-log scale) for heptane, micellar solution, water emulsions, and gel emulsions. The spreading factor decreases systematically with increasing viscosity. Gel emulsions exhibit a steeper power-law decay compared to water emulsions, suggesting additional microstructural resistance to spreading. Error bars represent the standard deviation from at least three independent impact experiments.

3.4 Evaporation of water-emulsions and gel-emulsions

Beyond impact and spreading, evaporation constitutes the final stage of the droplet dynamics under investigation. However, limitations in side-view imaging, such as the rapid evaporation rate and the accumulation of material near the droplet center, prevent reliable quantification of evaporation dynamics, including contact line recession, in emulsion systems. Therefore, we present bottom-view observations of drop deposition and film dewetting on the glass surface to gain further insights into the evaporation behavior.

Figures 5(a)-(b) depict bottom-view fluorescence images of drying drops containing either water emulsions (a) or gel emulsions (b) at 5, 10, and 25 vol.% aqueous phase. Each column corresponds to a different emulsion volume fraction, and each row represents a different time point during evaporation.

At early times ($t = 10$ s), the drop footprint is intact across all cases, showing uniform fluorescence from the micellar solution, where Span 80 micelles encapsulate either water or



352 gel. As *n*-heptane begins to evaporate, distinct dewetting patterns emerge. By $t = 60$ s,
353 water emulsion samples display increasingly heterogeneous structures, with radial fingering
354 and isolated micelle clusters more prominent at higher aqueous fractions. In contrast, gel
355 emulsions show more uniform deposition without pronounced radial features.

356 At late times ($t = 600$ s), the continuous *n*-heptane phase has fully evaporated, leaving
357 behind non-volatile Span 80 and the internal aqueous structures. Water emulsions produce
358 dispersed, near-circular deposits that remain mostly isolated. At 25 vol.%, the deposits
359 appear larger and more widely spaced, which may result from coalescence during the drying
360 process, from initial differences in emulsion packing and droplet stability, or from partial
361 evaporation of water from the internal phase. Partial water loss from the internal phase may
362 shrink droplets or promote coalescence during drying.

363 In gel emulsions, however, the final pattern differs significantly. Instead of discrete near-
364 circular deposits, the residual film fragments into irregular, branched, or network-like struc-
365 tures. These features become increasingly coarse and interconnected with higher gel content,
366 indicating that gelation within the internal phase inhibits droplet mobility and promotes
367 structural rigidity during drying.

368 High-magnification insets in the bottom two rows further confirm the morphological
369 contrast. Water emulsion residues show smooth, spherical features, while gel emulsions leave
370 behind rugged, interconnected deposits. These observations suggest that the rheological
371 properties of the internal phase (as discussed in the previous section) influence the final
372 dewetting morphology. The elastic and cohesive nature of the gel phase limits mobility,
373 resulting in structurally arrested films. Overall, the bottom-view imaging reveals that while
374 both systems undergo *n*-heptane evaporation and surfactant deposition, the internal phase
375 composition strongly influences the spatial organization of the residual film.



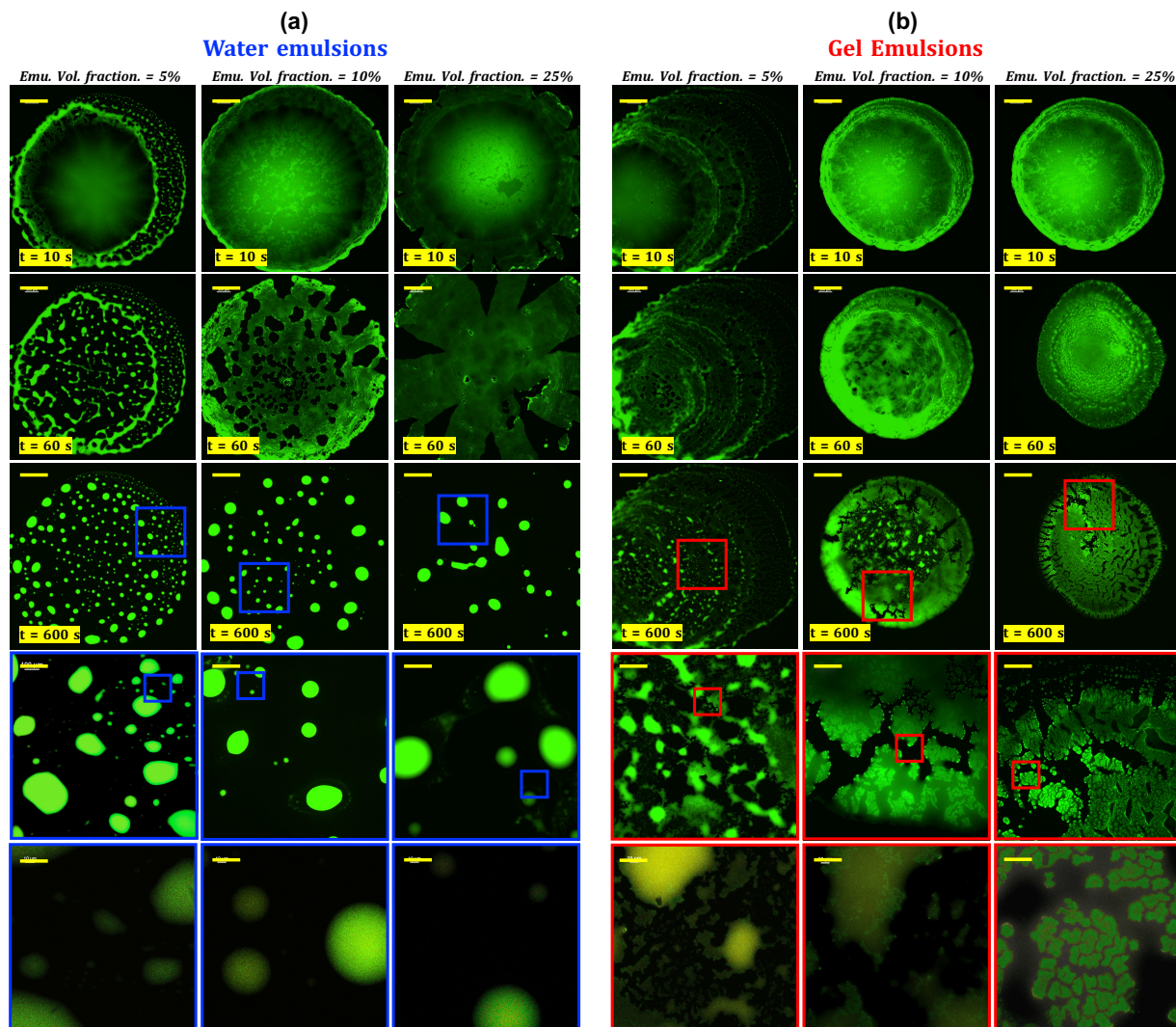


Figure 5: Bottom-view fluorescence images of drying drops containing (a) water emulsions and (b) gel emulsions at 5, 10, and 25 vol% aqueous phase. Each column corresponds to a different emulsion volume fraction. The top three rows show the temporal evolution of the drying drop at $t = 10$, 60, and 600 s (from top to bottom). The bottom three rows show increasing magnification of the boxed regions indicated in the third row ($t = 600$ s), with magnification increasing from top to bottom. As *n*-heptane evaporates, water emulsions form dispersed, near-circular deposits that become larger and more widely spaced at higher aqueous contents, possibly due to coalescence or water loss. In contrast, gel emulsions form irregular, interconnected structures, consistent with the presence of a more rigid internal phase. Scale bars are $1000 \mu\text{m}$ for the first three rows, and $200 \mu\text{m}$ and $30 \mu\text{m}$ for the lower rows (from top to bottom).



4. CONCLUSION

We investigated the dynamic behavior of emulsion-laden drops containing either water or gel as the internal phase, using *n*-heptane with Span 80 micelles as the continuous phase. By analyzing the process in distinct stages of impact, post-impact spreading, and drying/evaporation, we assess how internal phase state correlates with droplet evolution and final deposition. Within our experimental resolution, the impact dynamics are comparable for water and gel emulsions. For the impact-stage maximum spreading, a unified inertial–capillary–viscous correlation reproduces the measured spreading factors for single-phase liquids and water emulsions, while gel emulsions deviate at higher internal-phase fractions, suggesting additional dissipation not captured by a single effective-viscosity description. Gel emulsions consistently exhibit reduced late-stage spreading compared to water emulsions; this trend is consistent with higher effective dissipation associated with the gelled internal phase and the higher bulk viscosity of gel emulsions. Rheological measurements confirmed shear-thinning behavior in both systems, with gel emulsions showing significantly higher viscosity due to internal phase gelation.

During drying/evaporation, bottom-view imaging shows qualitatively different residue morphologies: water emulsions leave isolated, near-circular deposits, whereas gel emulsions form rugged, interconnected networks, consistent with reduced internal mobility and structural arrest during film breakup. Overall, the combined results suggest that internal rheological transitions can influence macroscopic spreading and deposition outcomes under our conditions. These insights are broadly relevant to fields such as inkjet printing, droplet-based coatings, and soft material processing, where control over deposit morphology is critical. Future work may explore how surfactant concentration, ambient humidity, or substrate properties interact with emulsion rheology to further tune final deposition patterns. In particular, it would be valuable to investigate how the rheological properties of the internal gel phase, including complex viscosity, elastic modulus, and potential yield stress, influence droplet impact dynamics.



ACKNOWLEDGMENT

The authors acknowledge financial support from CONACYT-SENER, managed by the National Council for Science and Technology of Mexico (CONACYT), the Natural Sciences and Engineering Research Council of Canada (NSERC) through a Discovery Grant (RGPIN-2025-05740), and the Department of National Defence (DND)/NSERC Discovery Grant Supplement. Additional support was provided by the University of Calgary's Canada First Research Excellence Fund (CFREF) Program and the Global Research Initiative for Sustainable Low-Carbon Unconventional Resources. Infrastructure funding from the Canada Foundation for Innovation (CFI) through CFI JELF Project No. 33700 is gratefully acknowledged.

References

- (1) Josserand, C.; Thoroddsen, S. Drop impact on a solid surface. *Annual Review of Fluid Mechanics* **2016**, *48*, 365–391.
- (2) Yu, Y.; Zhu, H.; Ozkan, H.; Derksen, R.; Krause, C. Evaporation and deposition coverage area of droplets containing insecticides and spray additives on hydrophilic, hydrophobic, and crabapple leaf surfaces. *Transactions of the American Society of Agricultural and Biological Engineers (ASABE)* **2009**, *52*, 39–49.
- (3) Yu, Y.; Zhu, J., H. Frantz; Reding, M.; Chan, K.; Ozkan, H. Evaporation and coverage area of pesticide droplets on hairy and waxy leaves. *Biosystems Engineering* **2009**, *104*, 324–334.
- (4) Auliano, M.; Auliano, D.; Fernandino, M.; Asinari, P.; Dorao, C. A. Can wicking control droplet cooling? *Langmuir* **2019**, *35*, 6562–6570.
- (5) Qi, W.; Weisensee, P. B. Dynamic wetting and heat transfer during droplet impact on bi-phobic wettability-patterned surfaces. *Physics of Fluids* **2020**, *32*, 067110.



- 427 (6) Bonn, D.; Eggers, J.; Indekeu, J.; Meunier, J.; Rolley, E. Wetting and spreading. *Re-*
428 *views of Modern Physics* **2009**, *81*, 739–805.
- 429 (7) Nyashina, G.; Vershinina, K. Y.; Strizhak, P. Impact of micro-explosive atomization
430 of fuel droplets on relative performance indicators of their combustion. *Fuel Processing*
431 *Technology* **2020**, *201*, 106334.
- 432 (8) Han, B.; Yun, G. Y.; Boley, J. W.; Kim, S. H.; Hwang, J. Y.; Chiu, G. T.-C.; Park, K.
433 Dropwise gelation-dehydration kinetics during drop-on-demand printing of hydrogel-
434 based materials. *International Journal of Heat and Mass Transfer* **2016**, *97*, 15–25.
- 435 (9) Jiao, Z.; Li, F.; Xie, L.; Liu, X.; Chi, B.; Yang, W. Experimental research of drop-on-
436 demand droplet jetting 3D printing with molten polymer. *Journal of Applied Polymer*
437 *Science* **2017**, *135*, 45933.
- 438 (10) Kettle, J.; Lamminmäki, T.; Gane, P. A review of modified surfaces for high speed
439 inkjet coating. *Surface and Coatings Technology* **2010**, *204*, 2103–2109.
- 440 (11) Leuner, C.; Dressman, J. Improving drug solubility for oral delivery using solid disper-
441 sions. *European Journal of Pharmaceutics and Biopharmaceutics* **2000**, *50*, 47–60.
- 442 (12) Kumar, A.; Mandal, D. K. Impact of emulsion drops on a solid surface: The effect of
443 viscosity. *Physics of Fluids* **2019**, *31*, 102106.
- 444 (13) Deblais, A.; Harich, R.; Bonn, D.; Colin, A.; Kellay, H. Spreading of an oil-in-water
445 emulsion on a glass plate: phase inversion and pattern formation. *Langmuir* **2015**, *31*,
446 5971–5981.
- 447 (14) Piskunov, M.; Semyonova, A.; Khomutov, N.; A., A.; Yanovsky, V. Effect of rheology
448 and interfacial tension on spreading of emulsion drops impacting a solid surface. *Physics*
449 *of Fluids* **2021**, *33*, 083309.



- 450 (15) Cordova-Gonzalez, M.; Hejazi, S. H. Integrating phase change materials and sponta-
451 neous emulsification: In-situ particle formation at oil–water interfaces. *Colloids and*
452 *Surfaces A: Physicochemical and Engineering Aspects* **2024**, *698*, 134439.
- 453 (16) Gonçalves, V.; Gurikov, P.; Poejo, J.; Matias, A.; Heinrich, S.; Duarte, C.; Smirnova, I.
454 Alginate-based hybrid aerogel microparticles for mucosal drug delivery. *European Jour-*
455 *nal of Pharmaceutics and Biopharmaceutics* **2016**, *107*, 160–170.
- 456 (17) Cardoso, C. O.; Ferreira-Nunes, R.; Cunha-Filho, M.; Gratieri, T.; Gelfuso, G. M. In
457 situ gelling microemulsion for topical ocular delivery of moxifloxacin and betametha-
458 sone. *Journal of Molecular Liquids* **2022**, *360*, 119559.
- 459 (18) Bhat, M.; Sakthikumar, R.; Sivakumar, D. Fuel drop impact on heated solid surface in
460 film evaporation regime. *Chemical Engineering Science* **2019**, *202*, 95–104.
- 461 (19) Semyonova, A.; Khomutov, N.; Misyura, S.; Piskunov, M. Dynamic and kinematic char-
462 acteristics of unsteady motion of a water-in-oil emulsion droplet in collision with a solid
463 heated wall under conditions of convective heat transfer. *International Communications*
464 *in Heat and Mass Transfer* **2022**, *137*, 106277.
- 465 (20) Kompinsky, E.; Dolan, G.; Sher, E. Experimental study on the dynamics of binary fuel
466 droplet impacts on a heated surface. *Chemical Engineering Science* **2013**, *98*, 186–194.
- 467 (21) Aytouna, M.; Bartolo, D.; Wegdam, G.; Bonn, D.; Rafai, S. Impact dynamics of sur-
468 factant laden drops: dynamic surface tension effects. *Experiments in Fluids* **2010**, *48*,
469 49–57.
- 470 (22) An, S. M.; Lee, S. Y. Maximum spreading of a shear-thinning liquid drop impacting on
471 dry solid surfaces. *Experimental Thermal and Fluid Science* **2012**, *38*, 140–148.
- 472 (23) Jambon-Puillet, E.; Carrier, O.; Shahidzadeh, N.; Brutin, D.; Eggers, J.; Bonn, D.



- 473 Spreading dynamics and contact angle of completely wetting volatile drops. *Journal of*
474 *Fluid Mechanics* **2018**, *844*, 817–830.
- 475 (24) Brinker, C. J.; Scherer, G. W. Sol → gel → glass: I. Gelation and gel structure. *Journal*
476 *of Non-Crystalline Solids* **1985**, *70*, 301–322.
- 477 (25) Katoueizadeh, E.; Rasouli, M.; Zebarjad, S. M. A comprehensive study on the gelation
478 process of silica gels from sodium silicate. *Journal of Materials Research and Technology*
479 **2020**, *9*, 10157–10165.
- 480 (26) Marsh, A. R., III; Klein, G.; Vermeulen, T. Polymerization kinetics and equilibria of
481 silicic acid in aqueous systems. *Technical Report* **1975**, 1–184.
- 482 (27) Sun, X.; Zhao, J.; Chen, T.; Liu, X. Colloidal particle size of fumed silica dispersed in
483 solution and the particle size effect on silica gelation and some electrochemical behaviour
484 in gelled electrolyte. *Journal of Solid State Electrochemistry* **2016**, *20*, 657–664.
- 485 (28) Pham, L. T.; Hatzignatiou, D. G. Rheological evaluation of a sodium silicate gel system
486 for water management in mature, naturally-fractured oilfields. *Journal of Petroleum*
487 *Science and Engineering* **2016**, *138*, 218–233.
- 488 (29) Gaboriaud, F.; Nonat, A.; Chaumont, D.; Craievich, A. Structural model of gelation
489 processes of a sodium silicate sol destabilized by calcium ions: combination of SAXS
490 and rheological measurements. *Journal of Non-Crystalline Solids* **2005**, *351*, 351–354.
- 491 (30) Koneva, A.; Safonova, E.; Kondrakhina, P.; Vovk, M.; Lezov, A.; Chernyshev, Y. S.;
492 Smirnova, N. Effect of water content on structural and phase behavior of water-in-oil (n-
493 decane) microemulsion system stabilized by mixed nonionic surfactants Span 80/Tween
494 80. *Colloids and Surfaces A: Physicochemical and Engineering Aspects* **2017**, *518*, 273–
495 282.



- 496 (31) Bazazi, P.; Hejazi, S. H. Spontaneous formation of double emulsions at particle-laden
497 interfaces. *Journal of Colloid and Interface Science* **2021**, *587*, 510–521.
- 498 (32) Bazazi, P.; Hejazi, S. H. Wetting dynamics of nanoparticle dispersions: from fully
499 spreading to non-sticking and the deposition of nanoparticle-laden surface droplets.
500 *ACS Applied Materials and Interfaces* **2022**, *14*, 20280–20290.
- 501 (33) Bazazi, P.; Stone, H. A.; Hejazi, S. H. Spongy all-in-liquid materials by in-situ formation
502 of emulsions at oil-water interfaces. *Nature Communications* **2022**, *13*, 4162.
- 503 (34) Bazazi, P.; Stone, H. A.; Hejazi, S. H. Dynamics of droplet pinch-Off at emulsified
504 oil-water interfaces: Interplay between interfacial viscoelasticity and capillary forces.
505 *Physical Review Letters* **2023**, *130*, 034001.
- 506 (35) Bazazi, P.; Stone, H. A. Pinch-off dynamics of emulsion filaments before and after
507 polymerization of the internal phase. *Soft Matter* **2025**, *21*, 1296–1307.
- 508 (36) Peltonen, L.; Hirvonen, J.; Yliruusi, J. The behavior of sorbitan surfactants at the
509 water-oil interface: Straight-chained hydrocarbons from pentane to dodecane as an oil
510 phase. *Journal of Colloid and Interface Science* **2001**, *240*, 272–276.
- 511 (37) Hayashi, K.; Shimanouchi, T.; Kato, K.; Miyazaki, T.; Nakamura, A.; Umakoshi, H.
512 Span 80 vesicles have a more fluid, flexible and wet surface than phospholipid liposomes.
513 *Colloids and Surfaces B: Biointerfaces* **2011**, *87*, 28–35.
- 514 (38) Ohama, Y.; Heike, Y.; Sugahara, T.; Sakata, K.; Yoshimura, N.; Hisaeda, Y.;
515 Hosokawa, M.; Takashima, S.; Kato, K. Gene transfection into HeLa cells by vesicles
516 containing cationic peptide lipid. *Bioscience, Biotechnology, and Biochemistry* **2005**,
517 *69*, 1453–1458.
- 518 (39) Bartolo, D.; Josserand, C.; Bonn, D. Singular jets and bubbles in drop impact. *Physical*
519 *Review Letters* **2006**, *96*, 124501.



- 520 (40) Modak, C.; Kumar, A.; Tripathy, A.; Prosenjit, S. Drop impact printing. *Nature Com-*
521 *munications* **2020**, *11*, 4327.
- 522 (41) Moghtadernejad, S.; Lee, C.; Jadidi, M. An introduction of droplet impact dynamics
523 to engineering students. *Fluids* **2020**, *5*, 107.
- 524 (42) Key reference: Gorin, B.; Di Mauro, G.; Bonn, D.; Kellay, H. Universal aspects of
525 droplet spreading dynamics in Newtonian and non-Newtonian fluids. *Langmuir* **2022**,
526 *38*, 2608–2613.
- 527 (43) Gordillo, J. M.; Riboux, G.; Quintero, E. S. A theory on the spreading of impacting
528 droplets. *Journal of Fluid Mechanics* **2019**, *866*, 298–315.
- 529 (44) Chandra, S.; di Marzo, M.; Qiao, Y. M.; Tartarini, P. Effect of liquid-solid contact
530 angle on droplet evaporation. *Fire Safety Journal* **1996**, *27*, 141–158.
- 531 (45) Shu, M.; Fan, L.; Zhang, J.; Li, J. Research progress of water-in-oil emulsion gelled
532 with internal aqueous phase: gel factors, gel mechanism, application fields, and future
533 direction of development. *Critical Reviews in Food Science and Nutrition* **2024**, *64*,
534 6055–6072.
- 535 (46) Sun, G.; Li, C.; Yang, F.; Yao, B.; Xiao, Z. Experimental investigation on the gelation
536 process and gel structure of water-in-waxy crude oil emulsion. *Energy & Fuels* **2017**,
537 *31*, 271–278.
- 538 (47) Mantovani, R. A.; Cavallieri, A. L. F.; Cunha, R. L. Gelation of oil-in-water emulsions
539 stabilized by whey protein. *Journal of Food Engineering* **2016**, *175*, 108–116.
- 540 (48) Liu, L.; Cai, G.; Wang, W.; He, B.; Tsai, P. A. On the maximum spreading of viscous
541 droplets impacting flat solid surfaces. *Journal of Fluid Mechanics* **2025**, *1018*, A42.
- 542 (49) Laan, N.; de Bruin, K. G.; Bartolo, D.; Josserand, C.; Bonn, D. Maximum diameter of
543 impacting liquid droplets. *Physical Review Applied* **2014**, *2*, 044018.



- 544 (50) Key reference: Sanjay, V.; Lohse, D. Unifying theory of scaling in drop impact: Forces
545 and maximum spreading diameter. *Physical Review Letters* **2025**, *134*, 104003.
- 546 (51) Key reference: Shah, P.; Driscoll, M. M. Drop impact dynamics of complex fluids: a
547 review. *Soft Matter* **2024**, *20*, 4839–4858.
- 548 (52) Nicolas, M. Spreading of a drop of neutrally buoyant suspension. *Journal of Fluid*
549 *Mechanics* **2005**, *545*, 271–280.
- 550 (53) Grishaev, V.; Iorio, C. S.; Dubois, F.; Amirfazli, A. Complex drop impact morphology.
551 *Langmuir* **2015**, *31*, 9833–9844.
- 552 (54) Boyer, F.; Sandoval-Nava, E.; Snoeijer, J. H.; Dijksman, J. F.; Lohse, D. Drop impact
553 of shear thickening liquids. *Physical Review Fluids* **2016**, *1*, 013901.



Data Availability Statement

The datasets generated and analyzed during the current study are available upon request. All experimental procedures and analysis protocols are described in detail within the manuscript and supporting information.

